

On the handling performance of a vehicle with different front-to-rear wheel torque distributions

LENZO, Basilio <<http://orcid.org/0000-0002-8520-7953>>, BUCCHI, Francesco, SORNIOTTI, Aldo and FRENDI, Francesco

Available from Sheffield Hallam University Research Archive (SHURA) at:

<https://shura.shu.ac.uk/23270/>

This document is the Accepted Version [AM]

Citation:

LENZO, Basilio, BUCCHI, Francesco, SORNIOTTI, Aldo and FRENDI, Francesco (2018). On the handling performance of a vehicle with different front-to-rear wheel torque distributions. *Vehicle System Dynamics*. [Article]

Copyright and re-use policy

See <http://shura.shu.ac.uk/information.html>

To appear in *Vehicle System Dynamics*
Vol. 00, No. 00, Month 20XX, 1–20

On the handling performance of a vehicle with different front-to-rear wheel torque distributions

Basilio Lenzo^{a*}, Francesco Bucchi^b, Aldo Sorniotti^c, and Francesco Frendo^b

^a*Department of Engineering and Mathematics, Sheffield Hallam University, Sheffield, UK;*

^b*Dipartimento di Ingegneria Civile e Industriale, Università di Pisa, Pisa, Italy;*

^c*Centre for Automotive Engineering, University of Surrey, Guildford, UK*

(Received 00 Month 20XX; accepted 00 Month 20XX)

The handling characteristic is a classical topic of vehicle dynamics. Usually, vehicle handling is studied through the analysis of the understeer coefficient in quasi-steady-state maneuvers. In this paper, experimental tests are performed on an electric vehicle with four independent motors, which is able to reproduce front-wheel-drive, rear-wheel-drive and all-wheel-drive (FWD, RWD and AWD, respectively) architectures. The handling characteristics of each architecture are inferred through classical and new concepts. More specifically, the study presents a procedure to compute the longitudinal and lateral tire forces, which is based on a first estimate and a subsequent correction of the tire forces that guarantee the equilibrium. A yaw moment analysis is then performed to identify the contributions of the longitudinal and lateral forces. The results show a good agreement between the classical and new formulations of the understeer coefficient, and allow to infer a relationship between the understeer coefficient and the yaw moment analysis. The handling characteristics for the considered maneuvers vary with the vehicle speed and front-to-rear wheel torque distribution. In particular, an apparently surprising result arises at low speed, where the RWD architecture is the most understeering configuration. This outcome is discussed through the yaw moment analysis, highlighting the yaw moment caused by the longitudinal forces of the front tires, which is significant for high values of lateral acceleration and steering angle.

Keywords: Electric vehicles, yaw moment, handling, understeer, experiments, ramp steer, FWD, RWD, AWD

1. Introduction

The handling characteristics of a vehicle are key factors for safety and performance. Vehicle models for the investigation of the vehicle cornering response have been developed since the 1960s [1, 2]. The concepts of handling diagram and understeer coefficient were introduced in [3], based on the linearized single-track vehicle model for steady-state cornering conditions. Further studies characterized the transient vehicle response, first by using the single-track model, and then with the progressive introduction of more advanced simulators, e.g., including non-linear tire force characteristics and suspension elasto-kinematics [4–8].

In recent years there has been a shift of focus from the characterization of the vehicle cornering response to its alteration, and even complete redesign according to specified criteria, by using vehicle dynamics control systems. For example, this can be achieved

*Corresponding author. Email: basilio.lenzo@shu.ac.uk

through direct yaw moment control (DYC), i.e., the generation of a yaw moment caused by different longitudinal tire forces on the left and right hand sides of the vehicle. In first instance, DYC was obtained with the individual control of the friction brakes, to achieve stability control in extreme transient conditions, e.g., during emergency maneuvers [9, 10]. More recently, the advent of electric vehicles led to new powertrain architectures, such as layouts with multiple motors, e.g., one per axle or one per wheel [11]. These configurations allow torque-vectoring, i.e., they can allocate desired torque levels to each electric motor. Several studies (for example, [12–15]) propose continuously active torque-vectoring controllers, with the purpose of designing the vehicle handling characteristic according to multiple driving modes selectable by the user. Such torque-vectoring-based DYCs were experimentally assessed on electric vehicles with multiple motors. These controllers require the design engineer to define reference yaw rate characteristics, which are based on the desired level of understeer [16, 17] and/or energy efficiency considerations [18–20], and depend on vehicle geometry, tire-road friction conditions [21], vehicle states, and driver inputs [16]. The reference yaw rate is usually compared online to the measured yaw rate, providing the basis for the calculation of the direct yaw moment [22]. In many cases the control strategy also considers the vehicle sideslip angle [14, 23], which can be either measured or estimated [24].

As discussed in [25, 26], the longitudinal tire forces affect the cornering response also in vehicle layouts without torque-vectoring capability, depending on the operating conditions. [27] simulates two-wheel-drive and four-wheel drive architectures with open differentials, and analyses the yaw moment effects of the longitudinal and lateral tire forces. Such contributions generate differences in the cornering response of the front-wheel-drive, rear-wheel-drive and all-wheel-drive (indicated as FWD, RWD and AWD in the remainder) modes of the same vehicle. In particular, in a steering pad maneuver the RWD configuration resulted more understeering than the FWD and AWD configurations, which is contrary to the common belief [28]. The understeer reduction in the FWD configuration is caused by the destabilizing yaw moment of the lateral component - in the vehicle reference system - of the front longitudinal tire forces in traction. [29] studies the impact of different drivetrain architectures on the handling diagram at high lateral accelerations, by considering a generic oversteering vehicle. In [30] a simple strategy is introduced to enhance maneuverability via appropriate wheel torque allocation, and FWD, RWD and AWD layouts are considered. These studies present only simulation results; to the best knowledge, the only preliminary experimental assessment is in the authors' previous work [31]. On a related topic, [27] proposes a new definition of understeer coefficient in quasi-steady-state maneuvers, yet again there is not any experimental application of such concept in the literature.

This papers aims to cover this gap with the following contributions:

- The experimental validation of the new definition of understeer coefficient, and its explicit relationship with the handling diagram;
- The computation of the tire forces starting from the vehicle test results, through a newly developed estimation and correction algorithm;
- The development of a vehicle model able to justify the experimental results, including a detailed analysis of the individual yaw moment contributions;
- The experimental assessment of the influence of the yaw moment on the cornering behaviour, with emphasis on the effects of the FWD, RWD and AWD modes on the measured handling diagrams.

The manuscript is organized as follows. Section 2 presents the test vehicle, the experimental tests and the adopted post-processing techniques. Section 3 focuses on the

Table 1.: Main vehicle parameters.

Symbol	Name and unit	Value
m	Mass (kg)	2290
J	Moment of inertia, vertical axis (kg m ²)	2761
a_1	Front semi-wheelbase (m)	1.365
l	Wheelbase (m)	2.665
τ	Transmission ratio (-)	10.56
R_w	Wheel radius (m)	0.364
t_1	Front track width (m)	1.616
t_2	Rear track width (m)	1.616
A_f	Frontal area (m ²)	2.69
C_x	Drag coefficient (-)	0.389
k_ϕ	Total roll stiffness (Nm/rad)	190000
$k_{\phi 1}$	Front axle roll stiffness (Nm/rad)	102600
$k_{\phi 2}$	Rear axle roll stiffness (Nm/rad)	87400
h	Center of mass height (m)	0.55
d_1	Front roll center height (m)	0.15
d_2	Rear roll center height (m)	0.15

numerical methods to estimate the tire-road forces, combining a mathematical model of the vehicle and tires with sensor measurements. Section 4 analyzes the theoretical and experimental results. Finally, the main conclusions are reported in Section 5.

2. Experimental tests

2.1. Test equipment and procedure

The experimental study was conducted at the Lommel proving ground (Belgium), on the electric Range Rover Evoque prototype (Figure 1) of the European project iCOMPOSE. The vehicle demonstrator features four identical on-board drivetrains, each of them consisting of a switched reluctance electric motor, a double-stage single-speed transmission system, constant velocity joints and a half-shaft. The main geometric and inertial parameters of the vehicle are reported in Table 1.



Figure 1.: The iCOMPOSE electric vehicle demonstrator with the Corrsys Datron sensor installed on the front end (Lommel proving ground, Belgium).

The test vehicle included the following sensors: i) a steering wheel angle sensor, measuring the steering wheel input applied by the driver, δ_w ; ii) a Corrsys Datron $S - 350$ sensor, installed on the front end of the car (see Figure 1), providing vehicle sideslip

angle, β_{DAT} , at the measurement location, and vehicle speed, V ; iii) an Inertial Measurement Unit (IMU), measuring the longitudinal acceleration, a_x , lateral acceleration, a_y , and yaw rate, r ; iv) wheel speed sensors, providing the angular speed of each wheel, i.e., ω_{ij} , with $i = 1, 2$ (front, rear) and $j = 1, 2$ (left, right); and v) battery current and voltage sensors.

The tests consisted of ramp steer maneuvers at 30 km/h, 60 km/h and 80 km/h. The desired vehicle speed was maintained throughout the maneuvers by means of a PI (Proportional Integral) speed tracking controller, providing the total motor torque demand, T_T , based on the difference between the reference speed and actual speed. The individual torque demands, T_{11} , T_{12} , T_{21} and T_{22} , were then calculated from T_T depending on the drivetrain architecture to be emulated, i.e. FWD, RWD and AWD with 50 – 50 front-to-rear distribution. The vehicle control software was implemented on a dSPACE AutoBox system. In all tests, the wheel torques were evenly distributed among the left- and right-hand sides of the vehicle. This guarantees that the different cornering responses are only caused by the yaw moment due to the different front-to-rear torque distributions, which reflects the purpose of this study.

The test protocol was the following:

- (1) The vehicle was accelerated from standstill to the reference speed in straight line, using the PI speed tracking controller;
- (2) Once the reference speed was reached, a steering wheel angle ramp was applied by the driver with approximately constant rate. A small value of steering wheel rate was selected, i.e. ≈ 2 deg/s, to make the vehicle operate close to its steady-state condition;
- (3) The test was considered completed when the vehicle yaw rate reached its saturation level;
- (4) Steps (1)-(3) were repeated for the selected vehicle speeds (30 km/h, 60 km/h and 80 km/h) and front-to-rear wheel torque distributions (FWD, RWD, AWD 50-50).

2.2. Signal processing and filtering

The relevant vehicle dynamics variables were obtained by combining the experimental measurements and vehicle kinematics, using the adapted ISO sign convention [32]. The value of sideslip angle at the center of mass of the vehicle, β (this location is the most commonly used in the literature, [14]), was calculated from the sideslip angle measured at the Datron sensor location, β_{DAT} , the yaw rate, r , and the longitudinal component of the velocity of the vehicle center of mass, u [33, 34]:

$$\tan \beta = \tan \beta_{\text{DAT}} - \frac{r}{u}(f + a_1) \quad (1)$$

where f is the longitudinal distance between the front axle of the vehicle and the Datron sensor.

The steering ratio of the car can be considered constant only in first approximation, for limited values of the steering wheel angle. Owing to the high steering angle values of these tests, an experimental non-linear map was used to estimate the steering angles of the left and right wheels, δ_{11} and δ_{12} , as functions of δ_w (Figure 2).

Appropriate filtering techniques were adopted to attenuate the effect of measurement noise. The input of the filtering process was the relevant part of the time history of each recorded signal, i.e. from when the driver applies the steering input to when the yaw rate saturates, as described in the test protocol. This was justified by the presence of swift

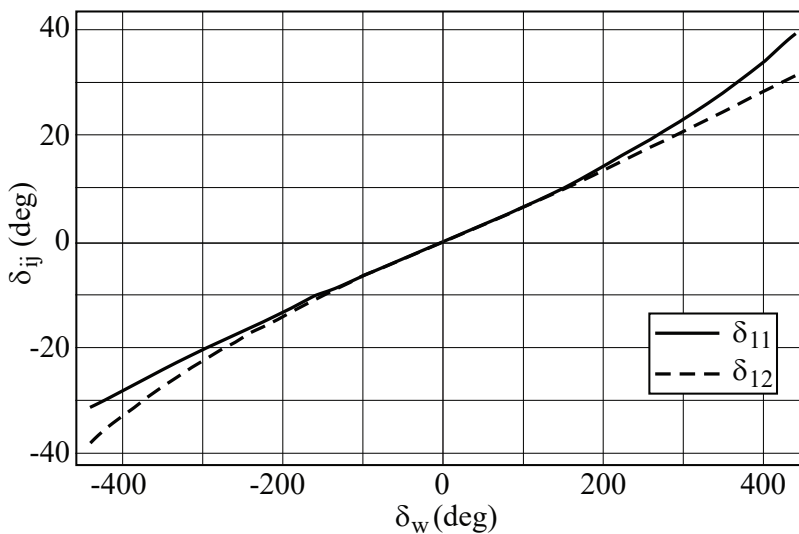


Figure 2.: Steering angle of the front left and front right wheel as functions of the steering wheel angle.

changes of the signals just outside their relevant part (e.g. see Figure 4). The Matlab "filtfilt" function was used, which executes a forward-backward filtering, averting phase lags. However, "filtfilt" might introduce undesired boundary effects at the beginning and/or end of the time window of the filtered signal. Where needed, such boundary effects have been addressed through:

Method 1 (M1), extending the time window of the signal to be filtered, by introducing fictitious data, i.e., a predetermined amount of reflected copies of the signal, at the beginning and/or at the end of the relevant part of the signal. To implement it in Matlab, it is sufficient to expand the vector of the signal to be filtered, by adding the fictitious data where relevant, then "filtfilt" is applied and the fictitious part of the filtered signal is removed;

Method 2 (M2), extending the time window of the signal to be filtered by a predetermined amount of time, at the beginning and/or at the end of the relevant part of the signal. To implement it in Matlab, it is sufficient to expand the vector of the signal to be filtered where relevant, and then apply "filtfilt". Finally, the extra part of the filtered signal is removed.

Based on the time history and the effect of each method, a careful analysis was performed for the measured signals. As a result, either M1, M2, or their combination, were adopted, with appropriate tuning parameters, i.e., the fictitious signal time length for M1, and the amount of extra time for M2. In particular, signal extensions were between 2 s and 5 s.

Figures 3 and 4 show examples of filtered functions, using "filtfilt" only (Basic filter, in the legend) and the combination of "filtfilt" and M1-M2. The vertical lines represent the boundaries of the relevant part of the test. Figure 3 shows the effect of the reflection of the signal (M1) at the end of a maneuver, due to the significant reduction of the sideslip angle at the end of the test. On the other hand, Figure 4 shows the benefit of the extension of the timeframe (M2) slightly before the beginning of the maneuver.

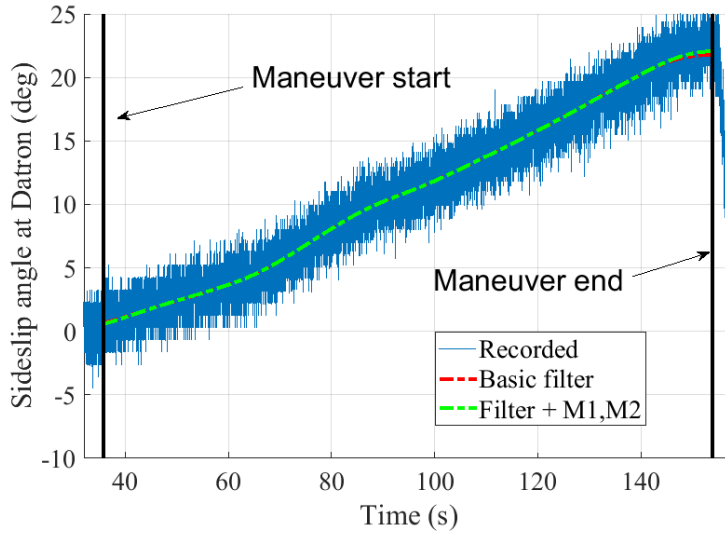


Figure 3.: Signal filtering: β_{DAT} for the 30 km/h AWD test.

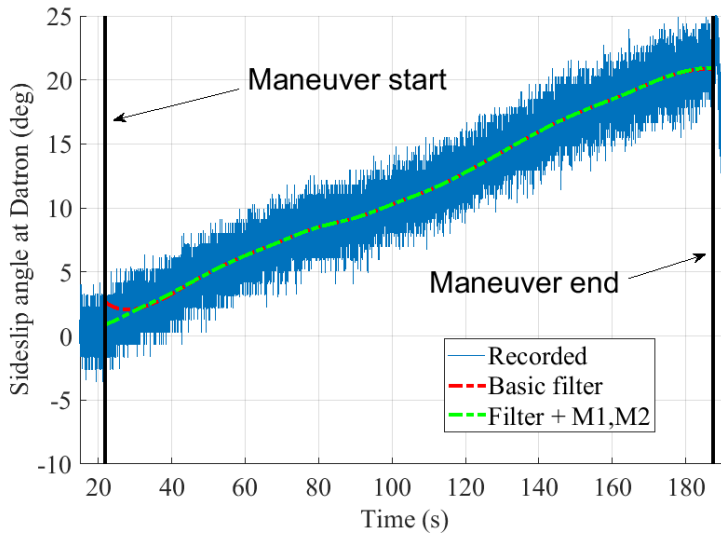


Figure 4.: Signal filtering: β_{DAT} for the 30 km/h RWD test.

3. Numerical models for tire force computation

The longitudinal and lateral forces of each tire are needed to assess the influence of the wheel torque distribution on vehicle dynamics [27]. However, the experimental measurements on the case study vehicle demonstrator do not directly provide such forces. Hence, a vehicle model is used to estimate the tire forces from the measured signals. In Section 3.1 the longitudinal forces are estimated from the time histories of the individual motor torque demands (T_{11} , T_{12} , T_{21} and T_{22}), while the lateral forces are estimated with a Pacejka tire model for pure cornering conditions, based on the time histories of estimated slip angle and vertical load on each corner. In Section 3.2 the vehicle force and yaw moment balance equations are considered, and the estimated longitudinal and lateral tire

forces are corrected to match the measured longitudinal, lateral and yaw accelerations at each time step.

3.1. Tire force estimation

The double track model in Figure 5 is used to assess the longitudinal and lateral tire forces starting from the experimental measurements. The model considers the vehicle as a rigid body with mass m and yaw moment of inertia J , moving on a flat surface. The forces acting on the rigid body are: i) the longitudinal tire forces, X_{ij} ; ii) the lateral tire forces, Y_{ij} ; and iii) the drag force, F_D , due to the aerodynamics and rolling resistance, which is assumed to be applied to the center of mass G . The self-aligning moments are neglected. δ_{11} and δ_{12} are the estimated steering angles of the front left and front right wheels, while the steering angles of the rear wheels are assumed to be zero. The vehicle geometry is assumed constant during the tests, and is described through the front and rear semi-wheelbases, a_1 and a_2 , the wheelbase, l , and the front and rear track widths, t_1 and t_2 .

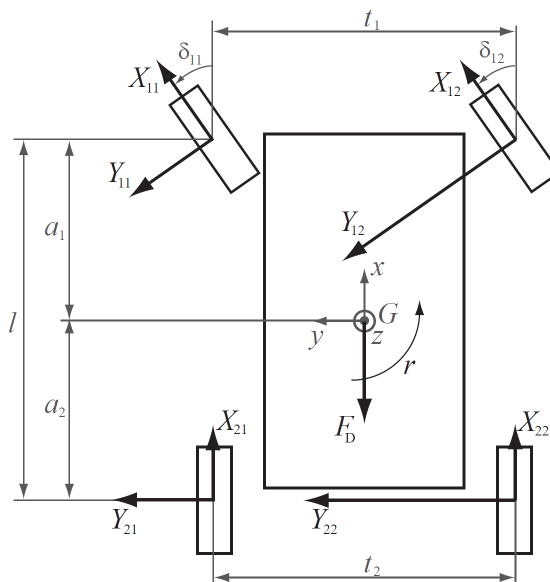


Figure 5.: Double-track vehicle model.

The longitudinal tire forces, X_{ij} , of the driving wheels are obtained from the respective motor torque, T_{ij} , by neglecting the inertial effects:

$$X_{ij} = \frac{\eta \tau T_{ij}}{R_w} \quad (2)$$

where τ is the motor-to-wheel transmission gear ratio and η is the efficiency of the electric motor and drivetrain. The longitudinal forces of the undriven wheels are assumed equal to 0.

The lateral forces, Y_{ij} , are assessed through the lateral force part of the Pacejka Magic

Formula, PAC2002 [32], neglecting camber angle and other secondary effects:

$$Y_{ij} = D \sin (C \arctan (B(\alpha_{ij} + S_{Hy}) - E(B(\alpha_{ij} + S_{Hy}) - \arctan B(\alpha_{ij} + S_{Hy})))) + S_{Vy} \quad (3)$$

where B , C and E are constant parameters, D depends on the vertical tire force, Z_{ij} , e.g. $D = \mu Z_{ij} \zeta_2$, μ is the tire-road friction coefficient, ζ_2 is a correction parameter, and S_{Hy} and S_{Vy} are curve translation parameters. The tire slip angles, α_{ij} , are computed with classical in-plane kinematics [33]:

$$\alpha_{ij} = \delta_{ij}^0 + \delta_{ij}(\delta_w) - \beta + (-1)^i a_i \frac{r}{u} \quad i = 1, 2; \quad j = 1, 2 \quad (4)$$

where δ_{ij}^0 is the static toe of each wheel, experimentally measured, and the relationship $\delta_{ij}(\delta_w)$ is known for the tested vehicle (Figure 2). The vertical loads, Z_{ij} , are assessed from the measured longitudinal and lateral accelerations of the vehicle center of mass, a_x and a_y :

$$Z_{ij} = \frac{mg(l - a_i)}{2l} + (-1)^i \frac{mh}{2l} a_x + (-1)^j \frac{ma_y}{t_i} \left(\frac{(l - a_i)d_i}{l} + \frac{k_{\phi i}}{k_{\phi 1} + k_{\phi 2}}(h - d) \right) \quad i = 1, 2; \quad j = 1, 2 \quad (5)$$

where g is the gravitational acceleration, $k_{\phi 1}$ and $k_{\phi 2}$ are the roll stiffness values of the front and rear suspensions, h is the center of mass height, d_i is the i -th roll center height, d is the height of the intersection point between the roll axis and a y - z plane through the center of mass.

The load transfer model is intentionally simple, such that no information on secondary effects, such as suspension geometry, actual tire-road friction coefficient and tire temperature, is required within the process. The outputs of this stage are corrected by the algorithm described in the following section.

3.2. Tire forces correction

By neglecting the static toe, the longitudinal, lateral and yaw balance equations of the vehicle model in Figure 5 are:

$$ma_x = X_{11} \cos \delta_{11} + X_{12} \cos \delta_{12} + X_{21} + X_{22} - Y_{11} \sin \delta_{11} - Y_{12} \sin \delta_{12} - F_D \quad (6a)$$

$$ma_y = Y_{11} \cos \delta_{11} + Y_{12} \cos \delta_{12} + Y_{21} + Y_{22} + X_{11} \sin \delta_{11} + X_{12} \sin \delta_{12} \quad (6b)$$

$$J\dot{r} = (Y_{11} \cos \delta_{11} + Y_{12} \cos \delta_{12} + X_{11} \sin \delta_{11} + X_{12} \sin \delta_{12})a_1 - (Y_{21} + Y_{22})a_2 + \\ + (X_{12} \cos \delta_{12} - X_{11} \cos \delta_{11})\frac{t_1}{2} + (X_{22} - X_{21})\frac{t_2}{2} + (Y_{11} \sin \delta_{11} - Y_{12} \sin \delta_{12})\frac{t_1}{2} \quad (6c)$$

As discussed in Section 2.1, a_x and a_y are measured by on-board accelerometers. The yaw acceleration, \dot{r} , can be derived from the measured yaw rate, r . The steering angles of the front left and front right wheels are computed from the measured steering wheel

angle, δ_w , through the steering law shown in Figure 2. The drag force, F_D , is:

$$F_D = \frac{1}{2}\gamma C_x A_f u^2 + F_R \quad (7)$$

where γ is the air density, C_x is the longitudinal aerodynamic drag coefficient, A_f is the vehicle frontal area, u is the longitudinal component of the velocity of the vehicle center of mass, and F_R is the total rolling resistance force, assumed constant.

Eq. 6 can be rewritten in the compact form $A\mathbf{x} = \mathbf{b}$, where the parameter matrix, A , is:

$$A = \begin{bmatrix} c_{\delta_{11}} & c_{\delta_{12}} & 1 & 1 & -s_{\delta_{11}} & -s_{\delta_{12}} & 0 & 0 \\ s_{\delta_{11}} & s_{\delta_{12}} & 0 & 0 & c_{\delta_{11}} & c_{\delta_{12}} & 1 & 1 \\ a_1 s_{\delta_{11}} - \frac{t_1}{2} c_{\delta_{11}} & a_1 s_{\delta_{12}} + \frac{t_1}{2} c_{\delta_{12}} & -\frac{t_2}{2} & \frac{t_2}{2} & a_1 c_{\delta_{11}} + \frac{t_1}{2} s_{\delta_{11}} & a_1 c_{\delta_{12}} - \frac{t_1}{2} s_{\delta_{12}} & -a_2 & -a_2 \end{bmatrix} \quad (8)$$

with cosine and sine functions abbreviated respectively as c and s . The estimated tire force vector, \mathbf{x} , is:

$$\mathbf{x} = [X_{11} \ X_{12} \ X_{21} \ X_{22} \ Y_{11} \ Y_{12} \ Y_{21} \ Y_{22}]^T \quad (9)$$

and the inertial and drag force vector, \mathbf{b} , is:

$$\mathbf{b} = [ma_x + F_D \ ma_y \ Jr]^T \quad (10)$$

At each time step: i) the elements of A are known from the measured steering wheel angle, the known steering law, and vehicle geometry; ii) the forces in \mathbf{b} are calculated from the measured longitudinal and lateral accelerations, yaw rate and drag force equation (Eq. 7); and iii) the tire forces, \mathbf{x} , are estimated as described in Section 3.1.

Due to the simplifying hypotheses introduced in the numerical model and the differences between the pure lateral part of the PAC2002 tire model and the actual tires on the car, the left and right terms in Eq. 6 are not equal in general. Hence, a vector $\Delta\mathbf{x}$ is introduced to correct the estimated tire forces, \mathbf{x} , such that the equilibrium is actually satisfied:

$$A(\mathbf{x} + \Delta\mathbf{x}) = \mathbf{b} \quad (11)$$

As A is not a square matrix, its pseudoinverse, $A^+ = A^T(AA^T)^{-1}$, is required to calculate $\Delta\mathbf{x}$:

$$\Delta\mathbf{x} = A^+(\mathbf{b} - A\mathbf{x}). \quad (12)$$

Owing to the pseudoinverse properties [35], $\Delta\mathbf{x}$ is the minimum norm vector that, added to \mathbf{x} , allows the equilibrium equations to be satisfied. Eq. 12 contemplates all the components of $\Delta\mathbf{x}$ in the same way, without considering that they may have different orders of magnitude. For example, if the lateral acceleration is high, the lateral forces at the inner tires are much lower than the lateral forces at the outer tires, because of the lateral load transfer. To obtain a more realistic estimation, a weight matrix W was introduced:

$$W = \begin{bmatrix} Z_{11}^{-1} & 0 & 0 & 0 & 0 & 0 & 0 & 0 \\ 0 & Z_{12}^{-1} & 0 & 0 & 0 & 0 & 0 & 0 \\ 0 & 0 & Z_{21}^{-1} & 0 & 0 & 0 & 0 & 0 \\ 0 & 0 & 0 & Z_{22}^{-1} & 0 & 0 & 0 & 0 \\ 0 & 0 & 0 & 0 & Z_{11}^{-1} & 0 & 0 & 0 \\ 0 & 0 & 0 & 0 & 0 & Z_{12}^{-1} & 0 & 0 \\ 0 & 0 & 0 & 0 & 0 & 0 & Z_{21}^{-1} & 0 \\ 0 & 0 & 0 & 0 & 0 & 0 & 0 & Z_{22}^{-1} \end{bmatrix} \quad (13)$$

Each diagonal element kk of W is the reciprocal of the vertical load acting on the tire considered in the k -th element of \mathbf{x} , e.g. $W_{33} = Z_{21}^{-1}$ because $\mathbf{x}_3 = X_{21}$ in Eq. 9. This normalizes the contribution of each element of $\Delta\mathbf{x}$, i.e., each correction term (k -th element of $\Delta\mathbf{x}$, see Eq. 9) is proportional to the actual vertical load Z_{ij} on that tire. In addition, two rows were added to the matrix A and to the vector \mathbf{b} to guarantee $X_{11} = X_{12}$ and $X_{21} = X_{22}$, which follows from the wheel torque allocation of the case study vehicle (see Section 2.1). The matrix A_1 and the vector \mathbf{b}_1 are then defined as:

$$A_1 = \begin{bmatrix} c_{\delta_{11}} & c_{\delta_{12}} & 1 & 1 & -s_{\delta_{11}} & -s_{\delta_{12}} & 0 & 0 \\ s_{\delta_{11}} & s_{\delta_{12}} & 0 & 0 & c_{\delta_{11}} & c_{\delta_{12}} & 1 & 1 \\ a_1 s_{\delta_{11}} - \frac{t_1}{2} c_{\delta_{11}} & a_1 s_{\delta_{12}} + \frac{t_1}{2} c_{\delta_{12}} & -\frac{t_2}{2} & \frac{t_2}{2} & a_1 c_{\delta_{11}} + \frac{t_1}{2} s_{\delta_{11}} & a_1 c_{\delta_{12}} - \frac{t_1}{2} s_{\delta_{12}} & -a_2 & -a_2 \\ 1 & -1 & 0 & 0 & 0 & 0 & 0 & 0 \\ 0 & 0 & 1 & -1 & 0 & 0 & 0 & 0 \end{bmatrix} \quad (14)$$

$$\mathbf{b}_1 = [ma_x + F_D \quad ma_y \quad Jr \quad 0 \quad 0]^T \quad (15)$$

The definitions of A_1 and \mathbf{b}_1 are valid for the AWD architecture, while only one additional row is necessary to guarantee $X_{11} = X_{12}$ for the FWD layout and $X_{21} = X_{22}$ for the RWD layout. The assumption of equal forces on the same axle is valid if the friction limit is not reached by any tire, otherwise dynamic equations for each wheel should be considered. The weight matrix is then introduced in the pseudoinverse definition [36]:

$$\tilde{A}_1^+ = W^{-1} A_1^T (A_1 W^{-1} A_1^T)^{-1} \quad (16)$$

therefore the associated tire force correction vector, $\Delta\tilde{\mathbf{x}}$, is computed as:

$$\Delta\tilde{\mathbf{x}} = \tilde{A}_1^+ (\mathbf{b}_1 - A_1 \mathbf{x}). \quad (17)$$

Finally, the corrected tire forces $\tilde{\mathbf{x}}$ are obtained as:

$$\tilde{\mathbf{x}} = \mathbf{x} + \Delta\tilde{\mathbf{x}}. \quad (18)$$

4. Results and discussion

This section discusses the results obtained directly from the experimental tests, and indirectly through the tire force estimation. Firstly, the understeer characteristics for each maneuver are derived, by using the classical and alternative definitions of understeer coefficient. Secondly, the tire forces are estimated and corrected with the procedure in Section 3. Such forces are used for the analysis of the different yaw moment components. Finally, the relationship between the understeer coefficient and the yaw moment is presented.

4.1. Understeer coefficients and handling diagram

To compare the handling of the vehicle for different speeds and drivetrain architectures, the understeer coefficient, K , is considered, using both the classical definition in [3] and the alternative definition proposed in [27], denoted as "new definition" in the remainder. In particular, the classical definition is:

$$K = \frac{\partial(\alpha_1 - \alpha_2)}{\partial \tilde{a}_y} \quad (19)$$

where α_1 and α_2 are the front and rear slip angles in the single-track model and $\tilde{a}_y = u^2 \rho$ is the steady-state lateral acceleration, where $\rho = r/u$. From the congruence equations of the single-track model, the understeer coefficient is

$$K = \frac{\partial(\bar{\delta} - l\rho)}{\partial \tilde{a}_y} = \frac{\partial \delta_{\text{dyn}}}{\partial \tilde{a}_y} \quad (20)$$

where $\bar{\delta}$ is the steering angle of the front wheel in the single-track model, which can be calculated as the average of the steering angles of the front wheels, i.e. $\bar{\delta}(\delta_w) = \frac{\delta_{11}(\delta_w) + \delta_{12}(\delta_w)}{2}$. As discussed in [27], the understeer coefficient can be computed considering a series of steady-state maneuvers at different lateral accelerations. Alternatively, the new definition of the understeer coefficient allows a good estimation of K during constant speed maneuvers at small constant steering angle rate $\dot{\bar{\delta}}$ (as described in Section 2.1):

$$K \simeq \frac{1}{u^2} \left(\frac{\dot{\bar{\delta}}}{\dot{\rho}} - l \right). \quad (21)$$

Figure 6 considers the ramp steer maneuver at 60 km/h for the RWD architecture and applies the classical and new definitions of understeer coefficient. As the maneuvers were performed in quasi-steady-state conditions, i.e., with a steering wheel angle rate of ≈ 2 deg/s, the understeer coefficient for the classical definition is computed from $a_y(t)$ instead of \tilde{a}_y . The plot confirms that the two formulations are equivalent for the whole range of lateral accelerations.

Figure 7 reports the dynamic steering angle as a function of lateral acceleration for the considered vehicle speeds. At a glance, the handling characteristics are grouped together based on the vehicle speed. The maneuvers performed at 30 km/h show an oversteering behavior ($K < 0$) up to ≈ 8 m/s², and then an understeering behavior up to the maneuver completion. On the other hand, the maneuvers at 60 km/h and 80 km/h exhibit an understeering behavior for the whole lateral acceleration range. When comparing the

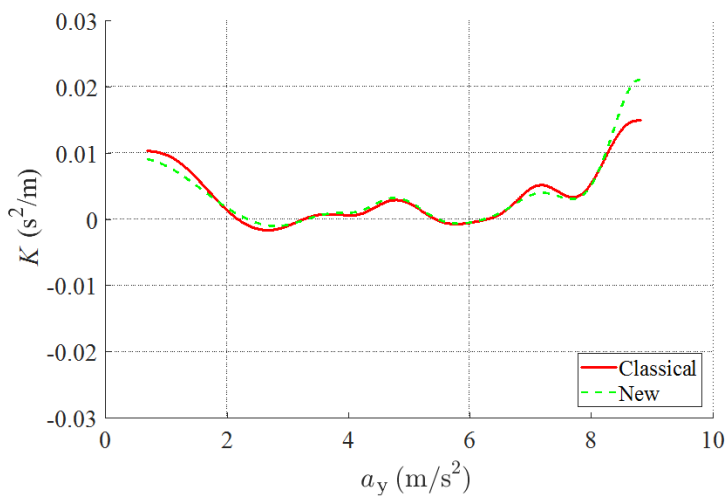


Figure 6.: Understeer coefficient according to the classical and new definitions for the 60 km/h RWD test.

maneuvers performed at the same speed, the resulting characteristics are very similar for the three architectures at 60 km/h and 80 km/h. A perceivable difference in the handling behavior of the three architectures is observed at 30 km/h and high a_y , where the RWD configuration is more understeering than the FWD and AWD ones.

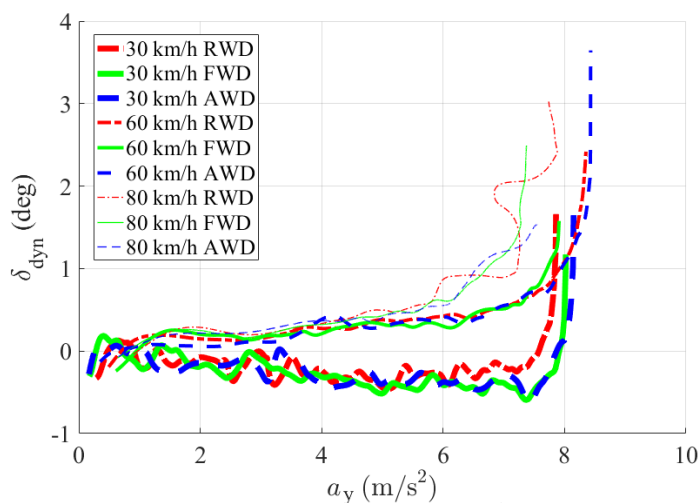


Figure 7.: Dynamic steering angle as a function of the vehicle lateral acceleration.

4.2. Tire force analysis

The longitudinal and lateral tire forces are computed for each test according to the procedure in Section 3. Considering the 60 km/h RWD test, Figure 8 shows the longitudinal forces, firstly estimated as described in Section 3.1, and then corrected to satisfy the force and moment balance equations, as described in Section 3.2. Figure 9 reports the

estimated and corrected lateral forces for the same test. The correction is small for the longitudinal forces of the driven wheels, while the undriven wheels are not shown because they do not exert any appreciable force. The lateral forces from the Pacejka model are generally lower than the corrected ones, especially at the rear tires for low lateral accelerations. The difference can be ascribed to the simplifying assumptions in the tire model considered for the estimation, where the secondary effects are neglected, e.g. camber and temperature, and the adherence factor is assumed equal to 1, without information on the actual tire-road friction coefficient. Moreover, the self-aligning moments are neglected in the vehicle model (Eq. 6). However, these assumptions are acceptable for a first approximated estimation of the forces, because the implemented correction guarantees the force and moment balance at the vehicle level.

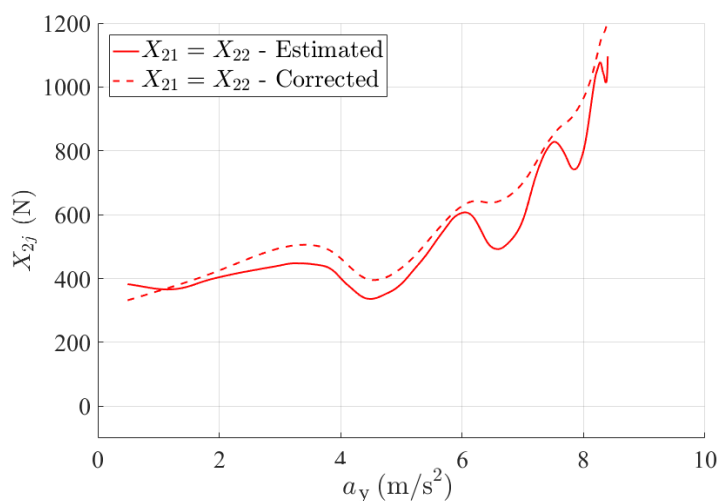


Figure 8.: Estimated and corrected longitudinal forces for the 60 km/h RWD test.

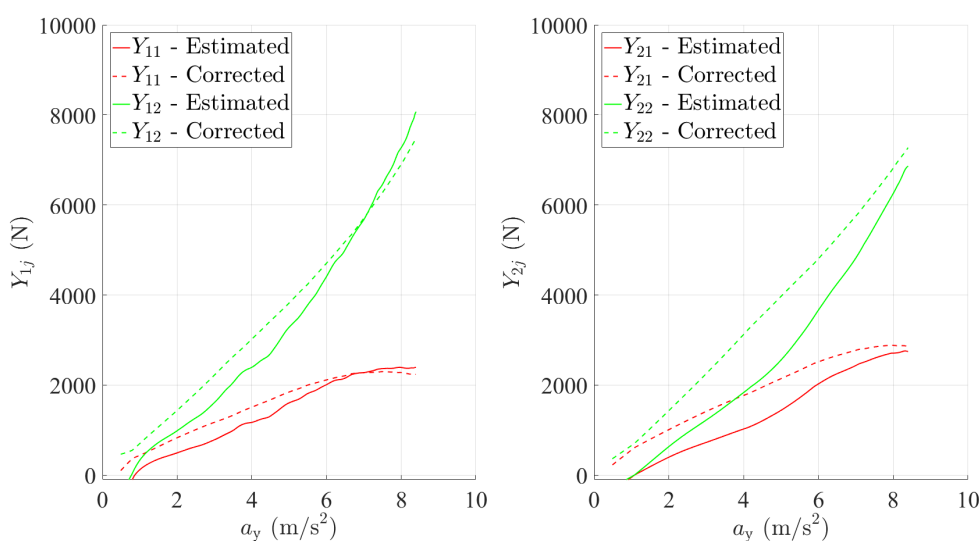


Figure 9.: Estimated and corrected lateral forces for the 60 km/h RWD test.

In order to verify that the corrected values of the forces did not overcome reasonable friction limits, the adherence index is computed as the ratio between the total tangential force exerted by each tire and the respective vertical load:

$$\mu_{ij} = \frac{\sqrt{X_{ij}^2 + Y_{ij}^2}}{Z_{ij}} \quad (22)$$

Figure 10 (right) shows the adherence index computed for all the tires during the ramp steer at 60 km/h with RWD layout. The maximum adherence is ≈ 1.15 for the internal tires and ≈ 0.8 for the external ones. This difference is caused by the dependence of the friction coefficient on the vertical load [34], i.e., the friction coefficient tends to decrease with the vertical load, which is higher on the external tires at high lateral accelerations. Figure 10 (left) shows the adherence index computed for the same test without introducing the weight matrix W , which is substituted by an identity matrix. In this case the results are slightly different, especially for the internal tires, where the adherence of the internal front tire is underestimated, while the adherence on the internal rear tire is overestimated. The weight matrix W was introduced to reduce the correction on tires with low vertical loads, by guaranteeing that the correction on those tires weighs more in the computation of the least square norm correction vector $\Delta\tilde{\mathbf{x}}$.

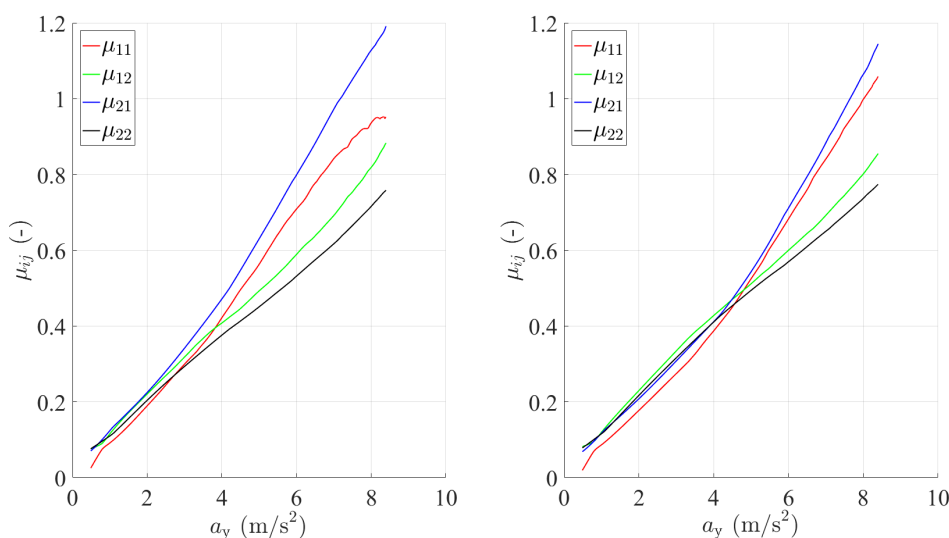


Figure 10.: Adherence index obtained by correcting the forces without (left) using the weight matrix W and (right) by using the weight matrix W , for the 60 km/h RWD test.

4.3. Yaw moment analysis

The total yaw moment, N , can be split into three terms, in accordance with the right-hand side of Eq. 6c:

$$N_f = X_{11}a_1 \sin \delta_{11} + X_{12}a_1 \sin \delta_{12} \quad (23)$$

$$N_y = Y_{11}(a_1 \cos \delta_{11} + \frac{t_1}{2} \sin \delta_{11}) + Y_{12}(a_1 \cos \delta_{12} - \frac{t_1}{2} \sin \delta_{12}) - (Y_{21} + Y_{22})a_2 \quad (24)$$

$$N_d = (X_{12} \cos \delta_{12} - X_{11} \cos \delta_{11}) \frac{t_1}{2} + (X_{22} - X_{21}) \frac{t_2}{2} \quad (25)$$

such that $J\dot{r} = N = N_f + N_y + N_d$. The term N_f is the yaw moment contribution of the longitudinal front tire forces along the y-axis of the vehicle reference system. The term N_y is the yaw moment contribution of the lateral forces acting on all tires. The term N_d is the yaw moment contribution related to the components of the longitudinal tire forces along the x-axis of the vehicle reference system. Under the assumptions $X_{11} = X_{12}$ and $X_{21} = X_{22}$, N_d is always nearly zero, except for high steering wheel angle values, when δ_{11} and δ_{12} are considerably different and, consequently, the term $X_{12} \cos \delta_{12} - X_{11} \cos \delta_{11}$ is not zero even if $X_{11} = X_{12}$.

Figure 11 shows the yaw moment contributions for all maneuvers. In the RWD architecture the only yaw moment contribution is N_y , as $N_f = 0$ because no longitudinal force is exerted by the front tires. As shown in Figure 11a, for the 30 km/h maneuver, N is almost constant in the whole lateral acceleration range, except at the end of the maneuver where N decreases. When considering higher speed maneuvers (Figure 11b and Figure 11c), N is higher at the beginning of the maneuver and decreases with the lateral acceleration, consistently with the yaw acceleration during the tests. In the FWD and AWD architectures, the contribution of N_f is very significant; in particular, N_f :

- Increases as the acceleration rises because, as discussed in [27] and [31], both the steering angles, δ_{11} and δ_{12} , and the longitudinal forces, X_{11} and X_{12} , increase;
- Is larger for low speed maneuvers, where, for a given value of lateral acceleration, the steering angle is larger;
- Is more pronounced in the maneuvers performed with the FWD architecture because the total longitudinal force is exerted only by the front tires, and thus X_{11} and X_{12} are greater than for the AWD configuration.

By adding all the yaw moment contributions, the total yaw moment N is obtained for all the maneuvers, as shown in Figure 12. Given a vehicle speed, the single yaw moment contributions in Figure 11 may have differences > 100 Nm. Even so, the total yaw moment is rather similar for all the architectures at a given speed, since the differences are within 10-20 Nm, and is affected by the driver behaviour during the test. Interestingly, for the 30 km/h maneuvers, in the FWD and AWD architectures N is greater than for the RWD architecture in the whole lateral acceleration range. In fact, with increasing lateral acceleration, the increase of N_f is larger than the decrease of N_y (see Figure 11).

In order to understand the relationship between the yaw moment plot and the understeer coefficient and, consequently, the dynamic steering angle (Figure 7), the definition of the understeer coefficient, as introduced in [27], is recalled:

$$K = \frac{\partial \delta_{dyn}}{\partial a_y} \simeq \frac{1}{u^2} \left(\frac{\dot{\delta}}{\dot{\rho}} - l \right) = \frac{1}{u^2} \left(\frac{\dot{\delta} u J}{N} - l \right) = \frac{\dot{\delta} J}{N u} - \frac{l}{u^2} \quad (26)$$

From this relationship it is clear that, for a given maneuver (defined by the time histories of $\dot{\delta}$ and u), the greater is N , the less understeering is the vehicle (lower K). Figure 13 reports the inverse of the yaw moment, i.e., $(1/N)$. Figure 13a shows that $1/N$ computed for the 30 km/h maneuver performed with the RWD architecture is always larger than

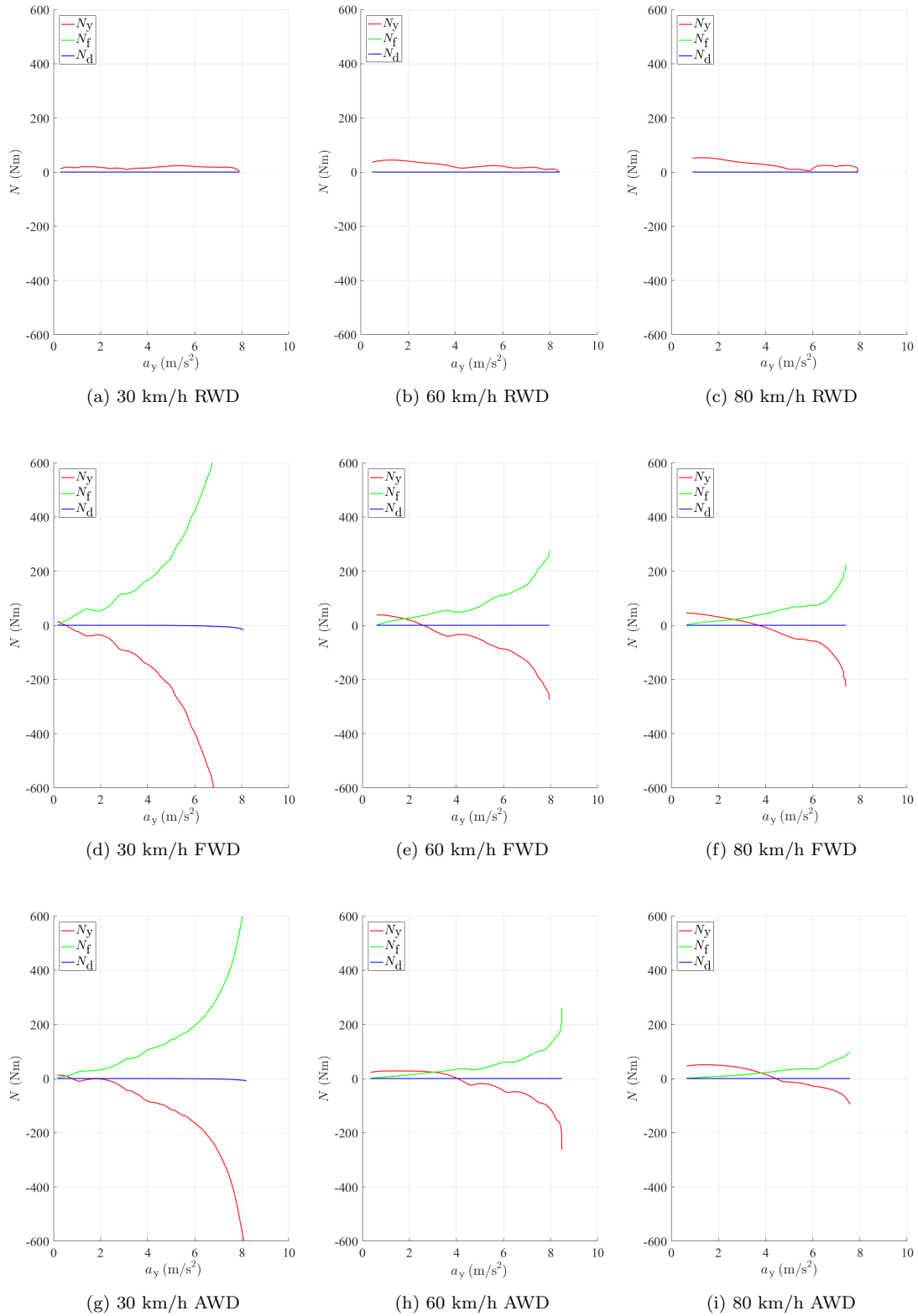


Figure 11.: Yaw moment contributions vs. lateral acceleration.

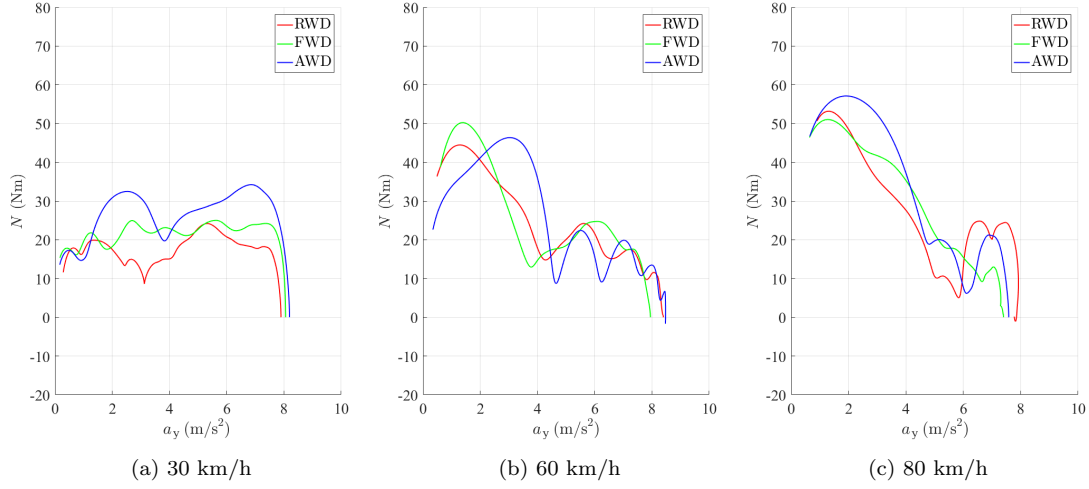


Figure 12.: Total yaw moment vs. lateral acceleration.

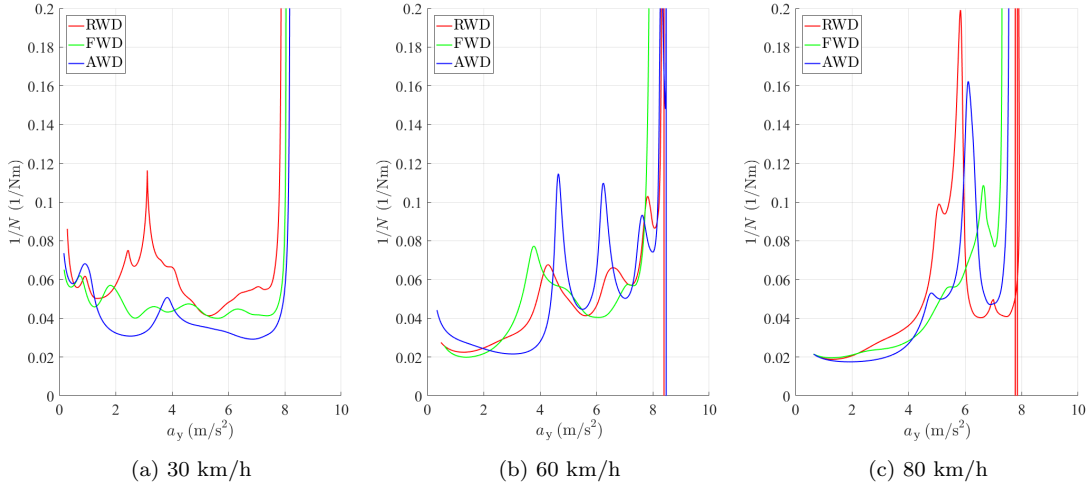


Figure 13.: Inverse of total yaw moment vs. lateral acceleration.

for the FWD and AWD architectures, confirming the more understeering behavior of the RWD set-up at 30 km/h. At higher speed maneuvers, no particular differences arise, which confirms Figure 7. It is worth remarking that N can be easily calculated from the yaw acceleration, \dot{r} , by multiplying it by J .

Finally, the relationship between the dynamic steering angle (Figure 7) and the total yaw moment is given by the following equation:

$$\delta_{dyn} = \int_0^{\bar{a}_y} K da_y = \int_0^{\bar{a}_y} \frac{\dot{\delta} J}{Nu} da_y - \int_0^{\bar{a}_y} \frac{l}{u^2} da_y = \dot{\delta} J \left(\frac{1}{u} \int_0^{\bar{a}_y} \frac{1}{N} da_y - \frac{l \bar{a}_y}{\dot{\delta} J u^2} \right) \quad (27)$$

which is obtained, for the first time, by integration of Eq. 26, considering quasi-steady-state conditions.

5. Conclusions

This paper compared the handling behavior of a vehicle equipped with four independent motors, which were controlled to emulate different drivetrain architectures. In particular, nine ramp steer tests were conducted at three different speeds, in the FWD, RWD and AWD modes. The cornering response was analyzed in terms of understeer coefficient and dynamic steering angle, as in the classical vehicle dynamics literature, with the additional consideration of the new formulation of the understeer coefficient proposed in [27]. A procedure to estimate and correct the longitudinal and lateral tire forces was presented. Based on the motor torque demands, a first estimate of the pure lateral tire force characteristics, and other measurements, the procedure finds a tire force distribution that satisfies the vehicle force and moment balance equations. A yaw moment analysis was performed with the obtained forces, to isolate the contributions of the longitudinal and lateral forces for the different maneuvers and operating modes. In particular, for the 30 km/h maneuver, a surprising result arised, as the RWD architecture resulted the most understeering. This can be ascribed to the destabilizing yaw moment produced by the longitudinal forces of the front tires, especially for high steering angles. Such yaw moment affects the vehicle dynamics in the FWD and AWD modes.

The results of this paper confirm the relationship between the classical handling analysis and the yaw moment analysis, which explains the effects of the longitudinal forces on vehicle dynamics in quasi-steady-state conditions.

6. Acknowledgement

The research leading to these results has received funding from the European Union Seventh Framework Programme FP7/2007-2013 under Grant Agreement No. 608897 (iCOMPOSE project).

References

- [1] Nordeen DL. Vehicle handling: Its dependence upon vehicle parameters. SAE Technical Paper; 1964. Report No.: 640108.
- [2] Sheridan TB. Vehicle handling: Mathematical characteristics of the driver. SAE Technical Paper; 1963. Report No.: 630068.
- [3] Pacejka HB. Simplified analysis of steady-state turning behaviour of motor vehicles. part 1. handling diagrams of simple systems. *Vehicle System Dynamics*. 1973;2(3):161–172.
- [4] Barter N. Analysis and interpretation of steady-state and transient vehicle response measurements. *Vehicle System Dynamics*. 1976;5(1-2):79–103.
- [5] VERMA MK. Transient response test procedures for measuring vehicle directional control. *Vehicle System Dynamics*. 1981;10(6):333–356.
- [6] Gim G. Vehicle dynamic simulation with a comprehensive model for pneumatic tires.. 1988;.
- [7] Farroni F, Russo M, Russo R, Terzo M, Timpone F. A combined use of phase plane and handling diagram method to study the influence of tyre and vehicle characteristics on stability. *Vehicle System Dynamics*. 2013;51(8):1265–1285.
- [8] Morales ED. Sensitivity study of front suspension parameters in elastokinematics and handling behavior of a vehicle. SAE Technical Paper; 2016. Report No.: 2016-36-0182.
- [9] Shibahata Y, Shimada K, Tomari T. Improvement of vehicle maneuverability by direct yaw moment control. *Vehicle System Dynamics*. 1993;22(5-6):465–481.
- [10] Van Zanten AT. Bosch esp systems: 5 years of experience. SAE Technical Paper; 2000. Report No.: 2000-01-1633.
- [11] De Novellis L, Sorniotti A, Gruber P. Design and comparison of the handling performance of different

- electric vehicle layouts. *Proceedings of the Institution of Mechanical Engineers, Part D: Journal of Automobile Engineering*. 2014;228(2):218–232.
- [12] Esmailzadeh E, Goodarzi A, Vossoughi G. Optimal yaw moment control law for improved vehicle handling. *Mechatronics*. 2003;13(7):659–675.
- [13] De Novellis L, Sorniotti A, Gruber P, Orus J, Fortun JMR, Theunissen J, De Smet J. Direct yaw moment control actuated through electric drivetrains and friction brakes: Theoretical design and experimental assessment. *Mechatronics*. 2015;26:1–15.
- [14] Lenzó B, Sorniotti A, Gruber P, Sannen K. On the experimental analysis of single input single output control of yaw rate and sideslip angle. *International Journal of Automotive Technology*. 2017;18(5):799–811.
- [15] Wang Z, Montanaro U, Fallah S, Sorniotti A, Lenzó B. A gain scheduled robust linear quadratic regulator for vehicle direct yaw moment control. *Mechatronics*. 2018;51:31–45.
- [16] De Novellis L, Sorniotti A, Gruber P. Driving modes for designing the cornering response of fully electric vehicles with multiple motors. *Mechanical Systems and Signal Processing*. 2015;64:1–15.
- [17] Lenzó B, Sorniotti A, De Filippis G, Gruber P, Sannen K. Understeer characteristics for energy-efficient fully electric vehicles with multiple motors. In: *EVS29 International Battery, Hybrid and Fuel Cell Electric Vehicle Symposium Proceedings*; 2016.
- [18] De Filippis G, Lenzó B, Sorniotti A, Gruber P, De Nijs W. Energy-efficient torque-vectoring control of electric vehicles with multiple drivetrains. *IEEE Transactions on Vehicular Technology*. 2018; 67(6):4702–4715.
- [19] Lenzó B, De Filippis G, Dizqah A, Sorniotti A, Gruber P, Fallah S, De Nijs W. Torque distribution strategies for energy-efficient electric vehicles with multiple drivetrains. *Journal of Dynamic Systems, Measurement, and Control*. 2017;139(12):121004.
- [20] Lin C, Xu Z. Wheel torque distribution of four-wheel-drive electric vehicles based on multi-objective optimization. *Energies*. 2015;8(5):3815–3831.
- [21] Farroni F, Lamberti R, Mancinelli N, Timpone F. Trip-id: A tool for a smart and interactive identification of magic formula tyre model parameters from experimental data acquired on track or test rig. *Mechanical Systems and Signal Processing*. 2018;102:1–22.
- [22] De Novellis L, Sorniotti A, Gruber P, Pennycott A. Comparison of feedback control techniques for torque-vectoring control of fully electric vehicles. *IEEE Transactions on Vehicular Technology*. 2014; 63(8):3612–3623.
- [23] Tota A, Lenzó B, Lu Q, Sorniotti A, Gruber P, Fallah S, Velardocchia M, Galvagno E, De Smet J. On the experimental analysis of integral sliding modes for yaw rate and sideslip control of an electric vehicle with multiple motors. *International Journal of Automotive Technology*. 2018;19(5):811–823.
- [24] Chindamo D, Lenzó B, Gadola M. On the vehicle sideslip angle estimation: A literature review of methods, models, and innovations. *Applied Sciences*. 2018;8(3):355.
- [25] Frenzo F, Greco G, Guiggiani M. Critical review of handling diagram and understeer gradient for vehicles with locked differential. *Vehicle System Dynamics*. 2006;44(06):431–447.
- [26] Frenzo F, Greco G, Guiggiani M, Sponziello A. The handling surface: a new perspective in vehicle dynamics. *Vehicle System Dynamics*. 2007;45(11):1001–1016.
- [27] Bucchi F, Frenzo F. A new formulation of the understeer coefficient to relate yaw torque and vehicle handling. *Vehicle System Dynamics*. 2016;54(6):831–847.
- [28] Osborn RP, Shim T. Independent control of all-wheel-drive torque distribution. *Vehicle system dynamics*. 2006;44(7):529–546.
- [29] Edelman J, Plochl M. Analysis of controllability of automobiles at steady-state cornering considering different drive concepts. *Proceedings of IAVSD 2017 (Dynamics of Vehicles on Roads and Tracks)*. 2017;.
- [30] Rill G. Reducing the cornering resistance by torque vectoring. *Procedia Engineering*. 2017;199:3284–3289.
- [31] Bucchi F, Lenzó B, Frenzo F, De Nijs W, Sorniotti A. The effect of the front-to-rear wheel torque distribution on vehicle handling: an experimental assessment. *Proceedings of IAVSD 2017 (Dynamics of Vehicles on Roads and Tracks)*. 2017;.
- [32] Pacejka H. *Tire and vehicle dynamics*. Elsevier; 2005.
- [33] Genta G. *Motor vehicle dynamics: modeling and simulation*. Vol. 43. World Scientific; 1997.
- [34] Guiggiani M. *The science of vehicle dynamics: handling, braking, and ride of road and race cars*. Springer Science & Business Media; 2014.
- [35] Moors E. On the reciprocal of the general algebraic matrix. *Bulletin of the American Mathematical Society*. 1920;9(26):394–95.
- [36] Ben-Israel A, Greville TN. *Generalized inverses: theory and applications*. Vol. 15. Springer Science

& Business Media; 2003.